Ore Geology Reviews 92 (2018) 29–41

Contents lists available at ScienceDirect

Ore Geology Reviews

journal homepage: www.elsevier.com/locate/oregeorev

NanoSIMS element mapping and sulfur isotope analysis of Au-bearing pyrite from Lannigou Carlin-type Au deposit in SW China: New insights into the origin and evolution of Au-bearing fluids

Jun Yan[a,b], Ruizhong Hu[a,b,*], Shen Liu[c], Yangting Lin[d], Jianchao Zhang[d], Shanling Fu[a]

[a] State Key Laboratory of Ore Deposit Geochemistry, Institute of Geochemistry, Chinese Academy of Sciences, Guiyang 550081, China
[b] University of Chinese Academy of Sciences, Beijing 100039, China
[c] State Key Laboratory of Continental Dynamics and Department of Geology, Northwest University, 229 Taibai Road, Xi'an 710069, China
[d] Key Laboratory of Earth and Planetary Physics, Institute of Geology and Geophysics, Chinese Academy of Sciences, Beijing 100029, China

ARTICLE INFO

Keywords:
Lannigou Au deposit
Carlin-type Au mineralization
NanoSIMS
Trace elements
Pyrite
Invisible gold
Sulfur isotopes

ABSTRACT

Sulfur isotope signatures of Au-bearing pyrite from Lannigou Au deposit, a typical Carlin-type Au deposit in SW China, provide valuable information about the origin of the ore-forming minerals. Analysis by NanoSIMS was used to determine S isotope compositions of Au-bearing pyrite and to map the grain-scale distributions of Au, Cu, As and S in pyrite from the deposit. Based on different textural pattern of pyrites revealed by back-scattered electron (BSE) images, they are divided into three types: Py-1 diagenetic pyrite without core-rim structure, Py-2 pyrite with an Au-free core and a rhythmically-zoned Au-bearing rim, Py-3 Au-bearing pyrite with rhythmic zoning across the entire grain. The element distributions and S isotope compositions of four paragenetic stages are recognized on the basis of textural observation. Py-1 grains and the Au-free homogeneous cores of zoned crystals were formed in Stage 1 while the Au-bearing rims of the zoned crystals with rhythmic zonation of As and Cu, and to a lesser degree Au, were formed in two superimposed stages: stage 2 formed the inner zone that is enriched in As alone; and stage 3 formed the outer zone that is enriched in both Au and As. Other sulfides such as realgar, cinnabar and stibnite are formed in the last stage. The relationship between Au and As distributions in pyrite rim is complicated, changing from coupled to decoupled at the nanoscale. Such complexity is interpreted to reflect fluctuation of fluid composition and temperature with time, which in turn affect the modes of occurrence of As and Au. It is inferred that As mainly occurs in the crystal lattice replacing S whereas Au is mainly present as nanoparticles that were trapped in pyrite during crystal growth. The Au-bearing rims of the zoned pyrite crystals are characterized by highly variable $\delta^{34}S$ values from 1.1 to 18.1‰, which exceed the values of the Triassic calcareous host rocks (10–14‰). In contrast, the $\delta^{34}S$ values of the Au-free cores of zoned pyrite crystals vary over a narrower interval and are mainly between 6 and 12‰, close to the values of pyrite crystals in the sedimentary country rocks. Our new analyses also reveals that the $\delta^{34}S$ values of the Au-bearing fluids generally increase during the formation of the deposit. The observed S isotope variations are consistent with mixing between a magmatic-related fluid with mantle-like $\delta^{34}S$ value (~0‰) and a sedimentary or deep basin brine fluid with elevated $\delta^{34}S$ value (> 18‰), with an increasing contribution from the latter with time. The notably varied values of $\delta^{34}S$ and the disseminations of Au and other trace elements such as As and Cu in pyrite crystals indicate that the process responsible for Au precipitation in this deposit occurred in an open hydrothermal system.

1. Introduction

Carlin-type gold deposits are best known in Nevada (USA) (Arehart, 1996; Hofstra and Cline, 2000) and SW China (Tu, 1990; Hu et al., 2002, 2017; Su et al., 2009a,b), and provide more than 9% of the global gold production (Cline et al., 2005; Price et al., 2008). Various analytical methods have been used to determine the compositions and sources of the ore-forming hydrothermal fluids for the Carlin-type Au deposits, including S isotope analysis of sulfides separates, H-O isotope analysis of fluid inclusions in quartz by crushing, C-O isotope analysis of calcite separates, *in-situ* measurements of trace element concentrations in a single fluid inclusion (e.g., Su et al., 2009a) and pyrite (e.g.,

* Corresponding author at: State Key Laboratory of Ore Deposit Geochemistry, Institute of Geochemistry, Chinese Academy of Sciences, Guiyang 550081, China.
E-mail address: huruizhong@vip.gyig.ac.cn (R. Hu).

https://doi.org/10.1016/j.oregeorev.2017.10.015
Received 1 May 2017; Received in revised form 15 September 2017; Accepted 16 October 2017
Available online 28 October 2017
0169-1368/

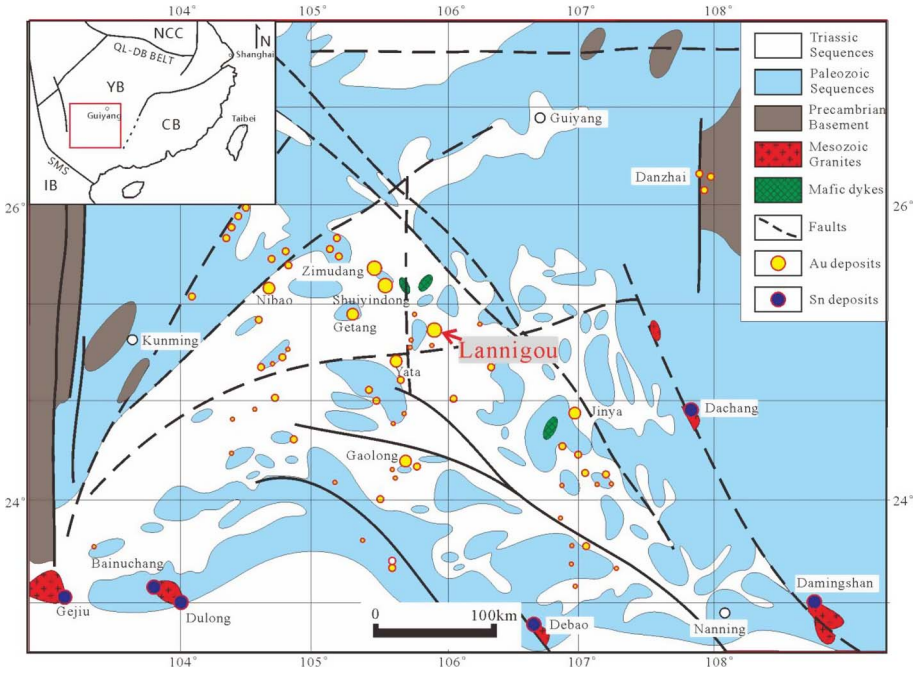

Fig. 1. Geologic map of the Dian-Qian-Gui region (also called Youjiang Basin) in SW China (after Hu and Zhou, 2012). NCB: North China Craton, YB: Yangtze Block, CB: Cathaysia Block, IB: Indochina Block, SMS: Song Ma Suture, QL-DB: Qinling-Dabie.

Large et al., 2009, 2011; Muntean et al., 2011) by Laser Ablation Inductively Coupled Plasma Mass Spectrometry (LA-ICP-MS), and *in-situ* measurements of S isotopes in pyrite and O isotopes in quartz by Secondary Ion Mass Spectrometry (SIMS) (e.g., Kesler et al., 2005; Lubben et al., 2012).

In contrast to study of ore-associated gangue minerals such as quartz and calcite, analysis of the main mineral hosting invisible gold (arsenian pyrite) provides direct information on the physic-chemical characteristics of the hydrothermal ore fluid. However, due to significant textural and compositional variation at a very fine scale (a few microns) within a single pyrite crystal in Carlin-type gold deposits, previous studies of gold-bearing pyrite were commonly hampered by high detection limits (electron microprobe, EMPA) or low spatial resolution of the analytical instruments (LA-ICPMS, SIMS) available in the past (Arehart et al., 1993; Kesler et al., 2003). These analytical limitations are now largely overcome by the development of NanoSIMS technologies that offer much higher spatial resolution down to the nanometer scales (~100 nm), coupled with low detection limits (down to a few ppm), compared to LA-ICPMS and EPMA respectively. Barker et al. (2009) are among the first researchers to utilize this new technique to study trace element distribution and $\delta^{34}S$ variations in a single Au-bearing pyrite crystal from the classical Carlin-type Au deposits in Nevada, western USA. Following their lead, we have used NanoSIMS to determine a uniquely clearer distribution of Au, As, Cu, S as well as the variation of $\delta^{34}S$ with higher spatial resolution across individual pyrite crystals from a representative Carlin-type Au deposit in SW China, the Lannigou Au deposit.

In contrast to characteristic isotope analyses of single minerals and LA-ICPMS trace elements analyses of gold-bearing pyrite, NanoSIMS can provide more detailed information of $\delta^{34}S$ and trace elements distributions with high spatial resolution. These data can be used to decipher the sources of ore-forming fluids and their chemical evolution over time in smaller temporal and spatial scale during mineralization.

2. Geological background

The South China block is located in the southeastern part of the Eurasian continent, which consists of the Yangtze block and the Cathaysia block, and bounded by the North China Craton to the north and by the Indochina block to the west. The Qinling-Dabie and Song Ma orogenic belts are the northern and western sutures that formed by Triassic continental collision (Zhou et al., 2006; Wang et al., 2007; Hu and Zhou, 2012; Hu et al., 2017; Fig. 1). The Dian-Qian-Gui region (also called Youjiang Basin) is the SW part of the Yangtze block, located at the junction of three provinces, Yunnan, Guizhou and Guangxi (Fig. 1). Since 1978, this region has been known to geologists as the “Golden Triangle” because there are many Carlin-type gold deposits in the region (Tu, 1992). Lithologically, the region is composed of Neoarchean to Neoproterozoic metamorphic rocks and Cambrian-Triassic carbonates and shales (Hu et al., 2002; Peters et al., 2007; Su et al., 2008; Hu and Zhou, 2012). Granite plutons with ages varying from Triassic (or Indosinian) to Jurassic-Cretaceous (or Yanshanian) are present at the fringes of the region as well as in the nearby regions to the east and south (Hu and Zhou, 2012; Mao et al., 2013; Pi et al., 2017; Zhu et al., 2017; Fig. 1).

The Lannigou (also known as Jinfeng) Au deposit is situated in the NW corner of the Laizishan anticline in the central part of the Golden Triangle. The deposit is a sediment-hosted disseminated gold deposit showing strong structural control. The major orebodies mainly occur as veins and lenses with disseminated-pyrite and quartz-veins in the steeply-dipping NW-trending F3, F6 fault, and the intersection of F3 fault and NE-striking F2 fault, or secondary faults linking with these major faults (Fig. 2). The deposit extends over 1200 m along its axis with a vertical extent up to 1100 m, and a thickness typically ranging from 10 to 50 m. The principal host units for ore body are the Middle Triassic calcareous siltstones and mudstones of the Bianyang and Xuman Formations. Gold is associated with arsenian pyrite, a major sulfide mineral of the Au-bearing quartz-sulfide veins. The Lannigou deposit is one of the largest Carlin-type Au deposits in the region, with a total Au resource estimated at > 5.3 million Oz, at an average grade of 4.5 g/t Au (Chen et al., 2011). The geology, mineralogy, fluid inclusions and stable isotopes have been studied previously (Hu et al., 2002; Wang et al., 2003; Zhang et al., 2003; Peters et al., 2007; Chen et al., 2011, 2015a,b; Gu et al., 2012; Xie et al., 2017). Previous results show some differences, e.g., formation temperature, as well as some similarities such as Au distribution between this deposit and the classical Carlin-type Au deposits in Nevada, USA (Hu et al., 2002; Xie et al., 2017).

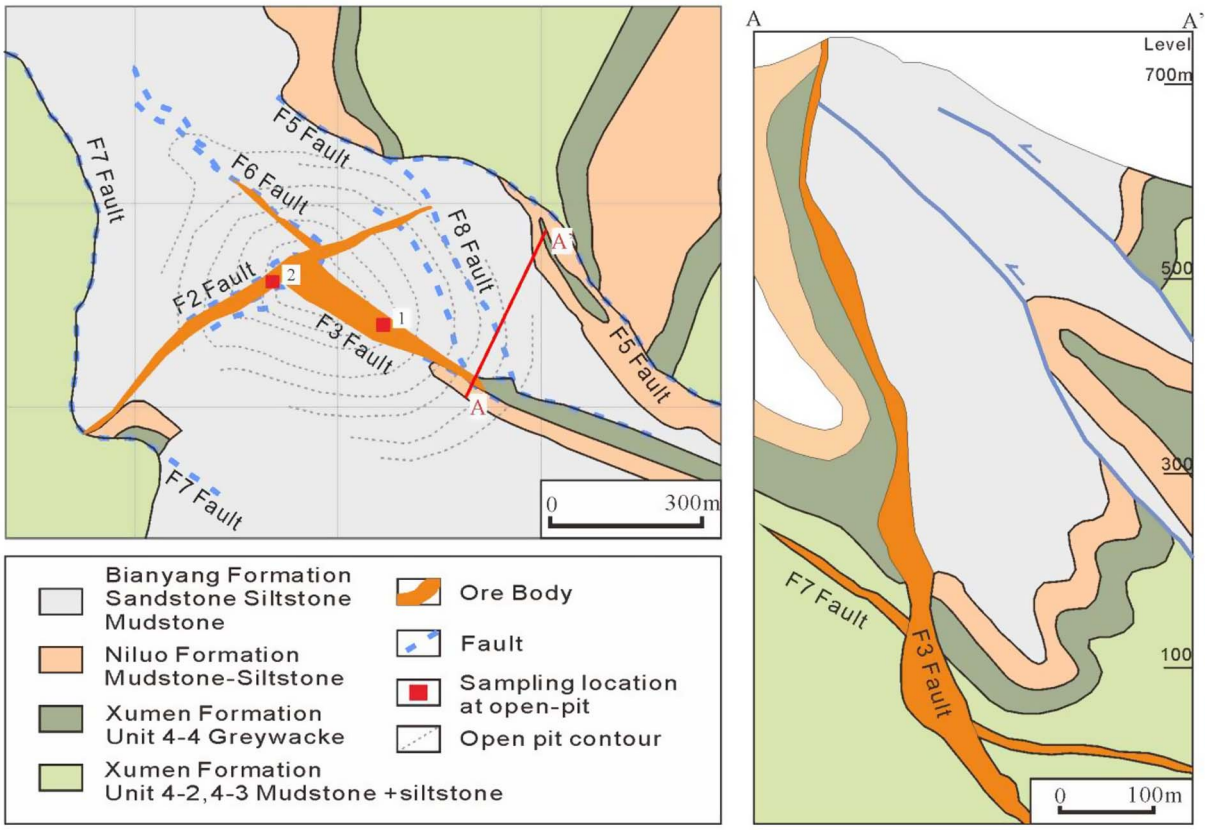

Fig. 2. Geology in plane (left) and in cross section A-A' (right) of Lannigou Carlin-type gold deposit (modified after Chen et al., 2011). The ore body is controlled by faults and mainly occurs steeply with F3 Fault. Red line A-A' in left map is cross section path.

3. Sampling and analytical methods

3.1. Samples

To obtain a more complete picture of the temporal and spatial evolution of the ore-forming hydrothermal fluids for the Lannigou Carlin-type Au deposit, samples from open-pit and underground workings were collected. Based on Au-grade, a series of samples were collected at two locations within the orebody exposed in the open-pit (Fig. 2) from 500 to 520 m level, and others were collected from ore heaps with different Au-grades from 250 to 370 m level (from underground). Detailed descriptions of the analyzed samples are given in Table 1. Among the collected samples, 7 of them are used for EPMA and 6 for *in-situ* S isotope and element mapping by NanoSIMS. Sulfur isotopes of sulfide separates such as realgar, stibnite and cinnabar of 10 samples analyzed by conventional methods, are used to evaluate sulfur isotope fractionation between coexisting minerals.

Table 1
Sampling location and details of samples.

Sample number	Description	Sampling location	Analysis methods
LNG3-1	Dark gray quartz veined breccia siltstone containing disseminated arsenopyrite	520 m level ore body at open-pit point 1	EPMA, NanoSIMS
LNG3-3			EPMA
LNG3-8	Low Au-grade quartz veined sandstone containing disseminated arsenopyrite	500 m level ore body at open-pit point 2	EPMA, NanoSIMS
LNG3-9	Quartz veined siltstone containing disseminated arsenopyrite, Au-grade increasing from 4.5 g/t to 6 g/t	250–370 m level at underground (ore heap samples)	EPMA, NanoSIMS
LNG3-11			EPMA, NanoSIMS
LNG3-12			EPMA, NanoSIMS
LNG6-1	Quartz veined siltstone containing cubic pyrite and calcite breccia	500 m level near ore body with very low Au-grade at open-pit point 2	EPMA, NanoSIMS
LNG-K-2	Milk quartz vein with stibnite containing siltstone breccia	250–370 m level at underground (ore heap samples)	Single mineral sulfur isotope
LNG-K-3	Dark gray quartz veined breccia siltstone, quartz containing little cinnabar, stibnite and realgar		
LNG-K-4	Dark gray quartz veined breccia siltstone, quartz containing little cinnabar, stibnite and realgar		
LNG-K-5	Black quartz veined mud-siltstone containing mass realgar		
LNG-K-6	Dark gray quartz veined siltstone containing little realgar and cinnabar		
LNG-K-8	Black quartz veined siltstone containing mass realgar and crystal quartz		
LNG-K-12	Coarse quartz vein containing mass realgar and crystal quartz		
LNG-K-13	Black quartz veined mud-siltstone containing mass realgar little cinnabar		
LNG-K-16	Coarse quartz vein containing little realgar and stibnite		
LNG-K-20	Milk quartz vein containing little cinnabar and stibnite		

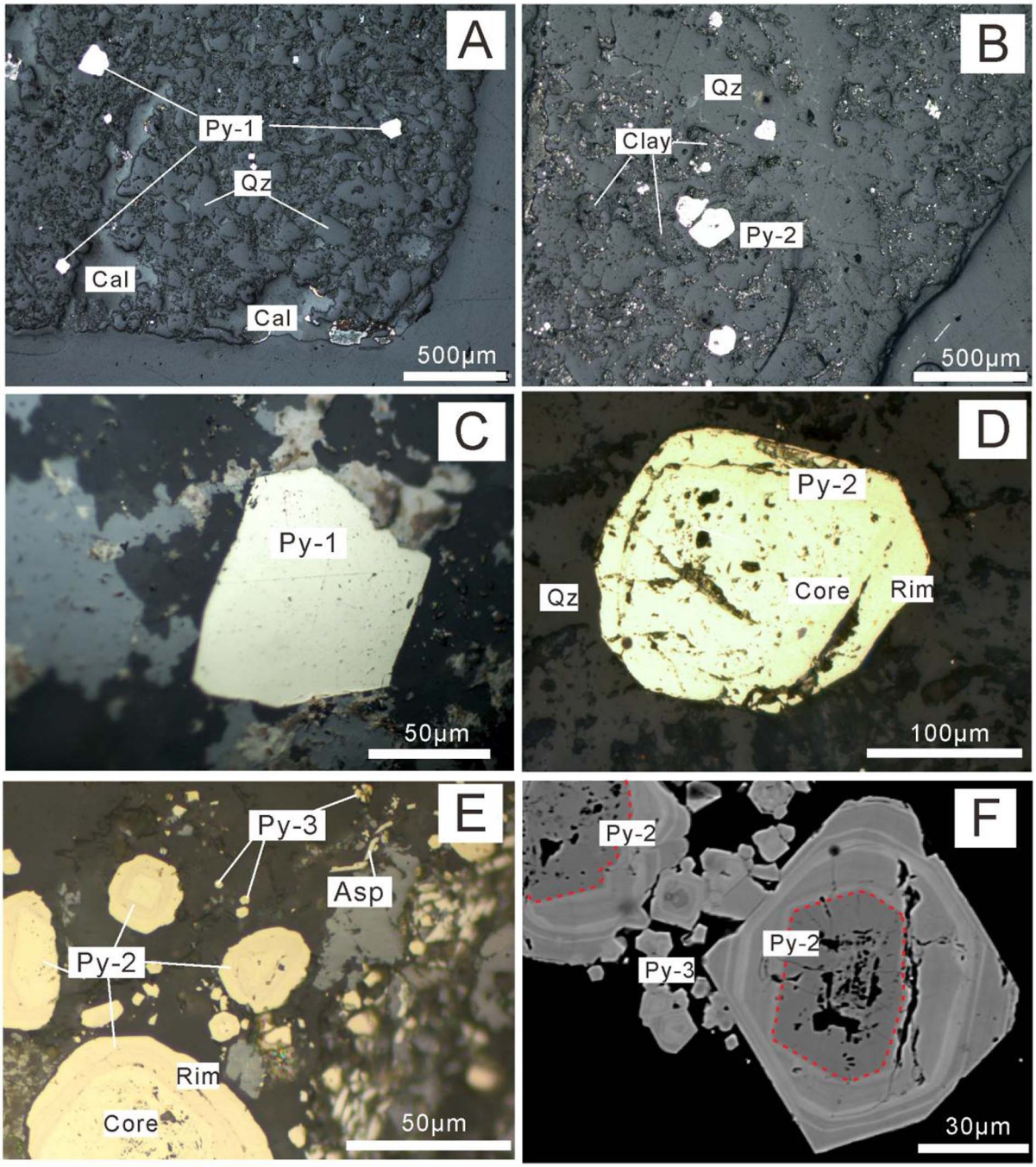

Fig. 3. Representative reflect light and BSE images of samples from Lannigou gold deposit. Mineral abbreviations: Py = pyrite, Qz = quartz, Cal = calcite, Asp = arsenopyrite. (A) Reflect light image of LNG6-1 from open pit near ore body. Most pyrites from this sample are As and Au barren. Calcite residues indicate incomplete decarbonization. (B) Reflect light image of LNG3-1 from open pit high grade Au ore. Gold-bearing pyrites are disseminated throughout sandstone with abundance quartz vein. (C) Reflect image of gold-barren pyrite Py-1. It shows a smooth surface and good crystallization. (D) (E) Reflect images of arsenic-pyrite Py-2 (with core-rim structure) and Py-3 (without core). The core-rim structure of Py-2 are revealed clearly under reflect light. (F) BSE images of arsenic-pyrite with core-rim structure Py-2 and tiny arsenic-pyrite Py-3. Rhythm sub-zonation is revealed in Py-2 rim and Py-3.

3.2. Methods

Polished thin sections were prepared from the samples used for the trace element and S isotope studies by NanoSIMS. Prior to the NanoSIMS analysis, the polished thin sections were carefully examined using optical microscope, SEM and EPMA to document the mineral assemblages, textures, major and minor element compositions of selected pyrites, and zonation of the selected pyrites at the submicron scales.

Secondary electron and BSE images were collected using a JEOL JSM7800F SEM under the operation conditions of 10 kV, 10 nA and a beam size of 1 μm in diameter, at the State Key Laboratory of Ore Deposit Geochemistry, Chinese Academy of Sciences, Guiyang.

Major and minor element compositions of the selected pyrites were determined using a JEOL JXA-8100 EMPA under the operation conditions of 15 kV, 10 nA and a beam size of 1 μm in diameter, count time 10 s (peak) and 5 s (upper and lower background), at the School of Earth Sciences and Resources, Chang'an University, Xi'an. The characteristic x-rays used are Fe (Kα), S (Kα), As (Lα), Au (Lα), Ni (Kα), Co (Kα), Cu (Kα) and Se (Lα). ZAF correction method was used for quantification. Standards, standard deviation 1 sigma (SD) and detection limits are detailed in Appendices I and II. The chemical

Table 2
EPMA geochemistry (wt.%) of the Lannigou pyrites rim, core and different stages in gold-bearing pyrites. Detection limits (wt.%) are shown below each element. n = number of analyzed spots.

Region/ stage	n	Fe (0.30)	Mean/SD (1σ)	S (0.20)	Mean/SD (1σ)	As (0.01)	Mean/SD (1σ)	Cu (0.01)	Mean/SD (1σ)	Ni (0.02)	Mean/SD (1σ)	Au (0.04)	Mean/SD (1σ)
Core	51	45.39–46.90	46.32/0.33	51.53–52.97	52.43/0.30	< 0.65	0.12/0.18	< 0.12	0.03/0.02	< 0.41	0.04/0.09	< 0.10	0.01/0.02
Rim	76	43.49–46.30	44.96/0.67	46.40–51.54	49.50/1.30	1.21–9.03	4.33/1.95	< 0.41	0.11/0.09	< 0.13	0.01/0.02	< 0.20	0.03/0.05
Stage 1	15	45.92–47.53	46.59/0.53	51.79–53.56	52.94/0.59	< 0.32	0.07/0.10	< 0.05	0.01/0.01	< 0.05	0.01/0.01	< 0.19	0.06/0.07
Stage 2	10	44.32–46.53	45.30/0.68	46.53–51.48	49.31/1.43	2.27–8.20	5.67/1.63	< 0.21	0.10/0.06	< 0.02	0.01/0.01	< 0.08	0.01/0.02
Stage 3a	25	44.47–46.68	45.49/0.59	48.25–52.50	50.64/0.99	1.20–6.52	3.46/1.23	< 0.21	0.09/0.05	< 0.04	0.01/0.01	< 0.28	0.08/0.08
Stage 3b	14	44.88–46.41	45.34/0.49	48.88–52.23	50.81/0.85	1.41–5.01	3.48/1.16	< 0.17	0.07/0.04	< 0.04	0.01/0.01	< 0.21	0.05/0.08

composition of pyrite core and Au-bearing rim were investigated before NanoSIMS analysis and chemical zonation of rim were also investigated more carefully by EPMA after NanoSIMS.

Trace element mapping (i.e., line or plane scan) and *in-situ* S isotope analysis of selected pyrite grains were conducted using a CAMECA NanoSIMS 50L instrument at the Institute of Geology and Geophysics, Chinese Academy of Sciences, Beijing. Samples were polished and coated with C for conductivity at high voltage. A primary Cs^+ ion beam of 1–2 pA and 100 nm in diameter was used for both types of analysis. The FC-EM-EM method of Zhang et al. (2014) was used for the *in-situ* S isotope analysis. ^{32}S was counted with Faraday cup (FC) to avoid the quasi-simultaneous arrival (QSA) effect and ^{34}S and other elements were counted with electronic multipliers (EMs). Certified international standards (including Pyrite of Balmat, CAR-123 pyrite) and working reference samples (pyrite PY-1117 and CS01) were used during S isotope analyses. Recommended $\delta^{34}S_{CDT}$ value of all standards are listed in Appendix I. The total count time for each S isotope analyses was 150 s, consisting of 300 cycles of 0.5 s. The sampling spot was 1–2 μm in diameter. The secondary electrons for ^{34}S, $^{63}Cu^{32}S$, ^{75}As, ^{80}Se, ^{197}Au and $^{208}Pb^{32}S$ were used for the elemental mapping. Peaks were calibrated using working references of chalcopyrite ($^{63}Cu^{32}S$), arsenopyrite (^{75}As), $FeSe_2$ (^{80}Se), Au foil (^{197}Au), galena ($^{208}Pb^{32}S$). A mass resolution of ~9000 (M/ΔM measured at 10% peak height) were achieved which is enough to eliminate the isobaric interferences of $^{32}SH_2^-$ and $^{33}SH^-$ on $^{34}S^-$, $^{32}S_5^{2-}$ and $^{32}S_2{}^{16}O^-$ on ^{80}Se-, $^{54}Fe_2{}^{57}Fe^{32}S^-$ and $^{32}S_4{}^{34}S_2H^-$ on $^{197}Au^-$, $^{56}Fe_2{}^{32}S_4^-$ on $^{208}Pb^{32}S^-$. It was noticed that

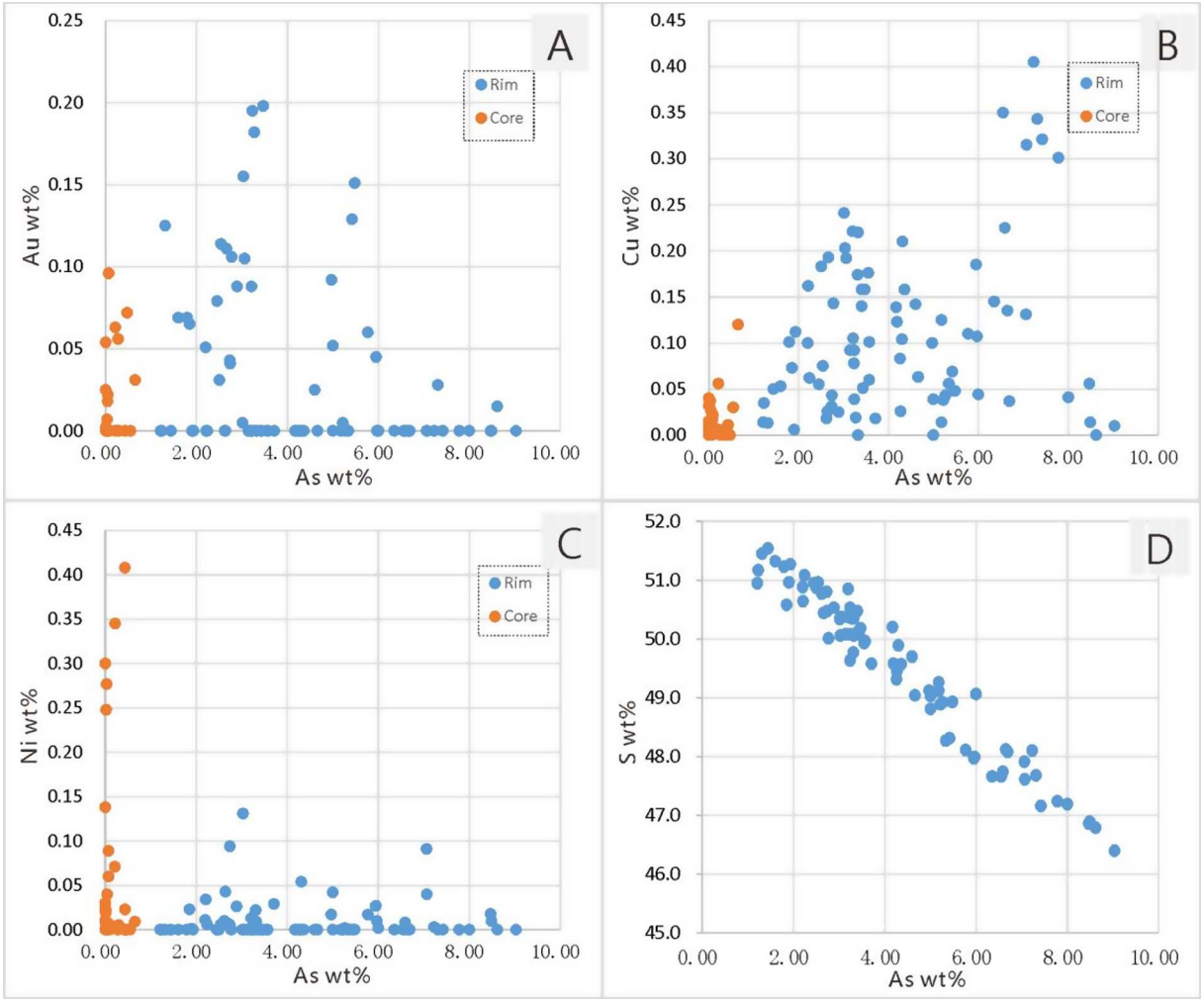

Fig. 4. EPMA geochemistry of pyrites core and rim before NanoSIMS analyses. Comparing with Au-barren core, pyrite Au-bearing rim is characterized by higher As, Cu and lower Ni concentration. Negative relationship between S and As indicates replacement of S by As.

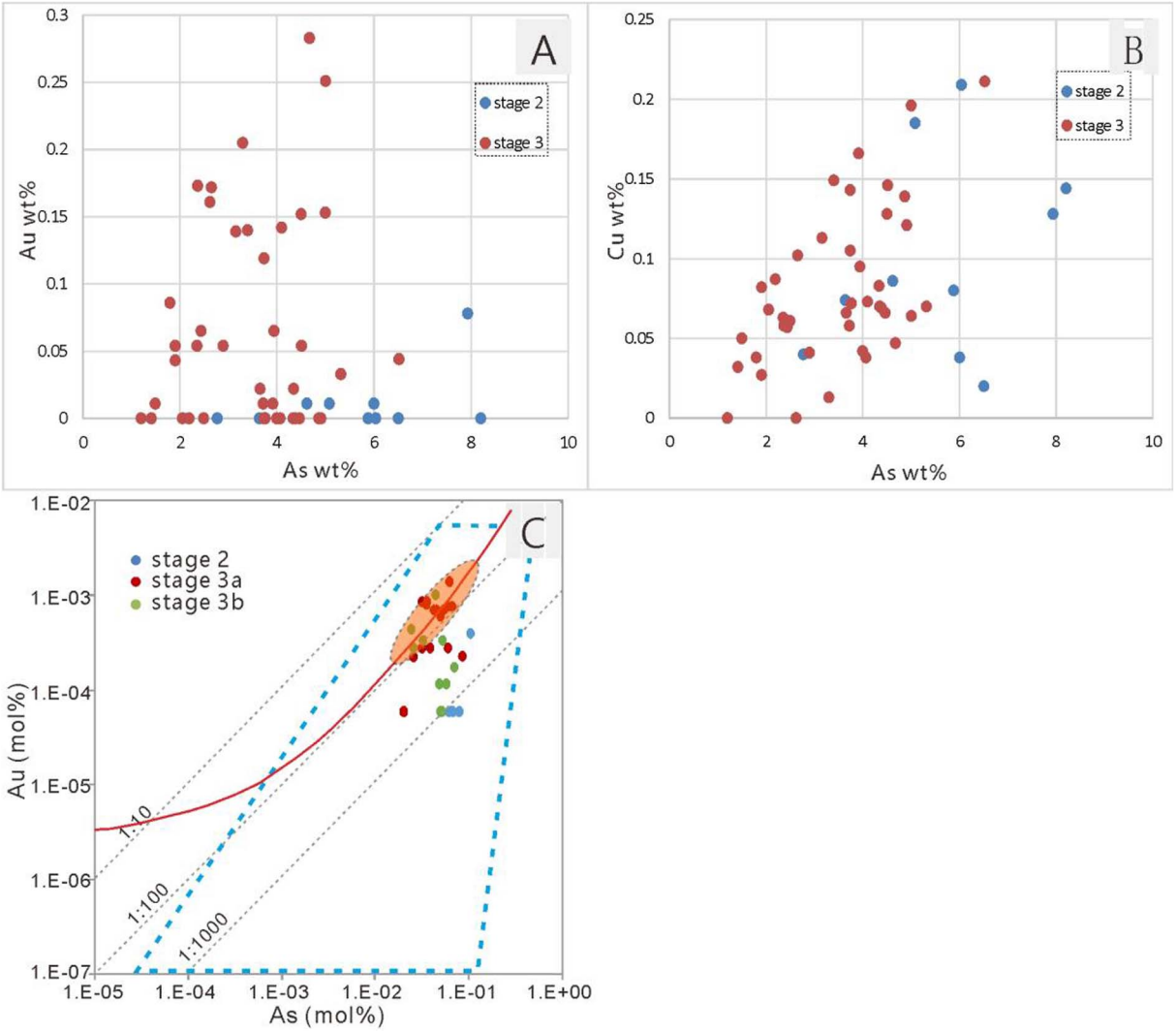

Fig. 5. EPMA analyses of stage 2 and stage 3 pyrites rim after NanoSIMS. Positive relationship between As and Cu (B) and huge variation of Au/As atom ratio (C) during gold-bearing pyrite precipitation are showed. Blue dashed line wedge zone in (C) is the Au: As atom ratio data of previous pyrites study in hydrothermal gold deposits by LA-ICPMS and SIMS (Deditius et al., 2014). Red line in (C) is solubility limit of Au in As-pyrite, and in orange ellipse zone, Au occurs as nanoparticles and/or Au^{+} (Reich et al., 2005). Dotted lines in (C) represent Au: As ratios (log-scale, in mol%).

the mass peak of $^{63}Cu^{32}S^{-}$ cannot be resolved from $^{95}Mo^{-}$. However, considering the concentration of Cu (hundreds ppm) and Mo (below detected limit of LA-ICPMS) in analyzed pyrites, the contribution of $^{95}Mo^{-}$ could be neglected. The color scales of the collected images represent relative signal intensities, not absolute concentrations, hence, different images are not comparable in the scales of signal intensities. The image size is 25 × 25 μm or 50 × 50 μm and the corresponding resolution is 256 × 256 or 512 × 512 pixels.

The S isotopes of stibnite, realgar and cinnabar separates were measured using the MAT-253 mass spectrometer at the State Key Laboratory of Environmental Geochemistry, Institute of Geochemistry, Chinese Academy of Sciences, Guiyang. Sulfur isotopic compositions of sulfide minerals were measured using the conventional combustion method and reported as $\delta^{34}S$ relative to VCDT. Working standards are GBW04414, GBW04415 and IAEA-S3.

4. Results

4.1. Paragenesis and compositional variation of pyrite

Based on mineral assemblages and textures, pyrite in the Lannigou deposit can be classified into three types: a precursor formed before hydrothermal mineralization (Py-1), a composite type with an inherited Au-free core and an overgrown Au-bearing rim (Py-2), and Au-bearing fine-grained pyrite without an Au-free core (Py-3). The Au in the deposit is mainly hosted in Py-3 and in the rims of Py-2 (Zhang et al., 2003). The textures of the different types of pyrite are illustrated in Fig. 3.

Among the samples used in this study, Py-1 is present only in the sample (LNG6-1) from the low Au-grade quartz veined siltstone near the orebody associated with the F6 fault. In this sample, residual calcite and anhedral quartz are also present (Fig. 3A). The residual calcite was thought to be evidence for decarbonization prior to Au deposition (Hu et al., 2002; Zhang et al., 2003). Py-1 is characterized by a cubic shape, smooth outline and homogeneous composition (Fig. 3C).

Py-2 (> 50 μm in diameter) and Py-3 (< 30 μm in diameter) are mainly present in the Au-bearing quartz-pyrite veins associated with the F3 fault. In more details, these types of pyrite are disseminated in the siltstone-mudstone fragments cut by small quartz veins (< 5 mm across) and to a lesser extent, in larger quartz veins (Fig. 3B). Compared to Py-1, Py-2 tends to have more cavities in its core (Fig. 3D–F). However, both Py-1 and the core of Py-2 have homogeneous composition. In contrast, the rim of Py-2 is characterized by oscillatory compositional zonation (Fig. 3F). Similarly, the entire grain of Py-3 also has

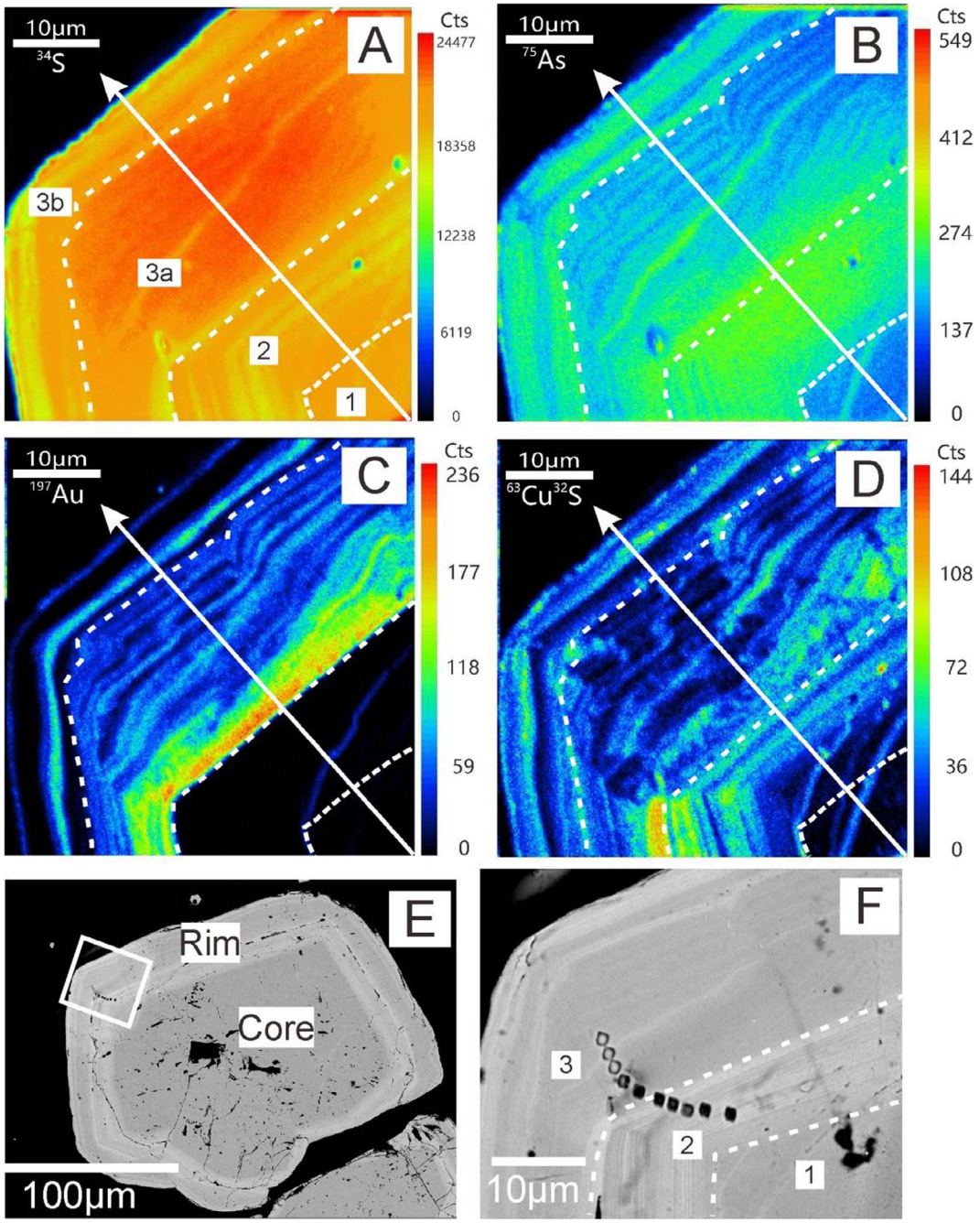

Fig. 6. NanoSIMS elements mapping of representative pyrite from sample LNG3-1, Lannigou gold deposit. LNG3-1 is collected at open pit ore body with 520m level. (A-D) are element mapping of ^{34}S, ^{75}As, ^{197}Au and $^{63}Cu^{32}S$ (represent ^{63}Cu) respectively. (E-F) are BSE images of analyzed pyrite. Three main stage can be distinguished by Au-As concentration and texture. Stage 1, pre-ore stage equal to pyrite core forming; stage 2, As precipitated without Au; stage 3, main Au precipitation stage. Two period in stage 3 are divided by line scan character of gold and arsenic. $^{63}Cu^{32}S$ was used for copper mapping instead of ^{63}Cu due to higher productivity. Color scale of these maps are linear. Frame in (E) is element mapping area. The white arrow denotes the path of line scan shown in Fig. 8A.

oscillatory compositional zonation (Fig. 3F).

Major and minor elements of these pyrites determined before NanoSIMS analyses are listed in Appendix II. Arsenic concentrations in Py-1 are < 0.69 wt%, Cu < 0.13 wt%. The core of Py-2 contains < 0.65 wt% As, < 0.06 wt% Cu and < 0.41 wt% Ni. In contrast, the Py-2 rim and Py-3 contain 1.31–10.84 wt% As, < 0.41 wt% Cu and < 0.13 wt% Ni. Due to similar concentration of As and Cu, Py-1 was considered the same as the core of Py-2, and Py-3 the same as the rim of Py-2. The chemical characteristics of core and rim are shown in Table 2 and Fig. 4. Distinct from the good positive correlation between Au and As concentrations in ore, the Au in pyrite shows a lack of linear correlation with As (Fig. 4A). However, Cu is positively correlated with As (Fig. 4B), and S is negatively correlated with As (Fig. 4D) which indicates replacement of S by As.

4.2. Nano-scale elemental and S-isotopic zonation of pyrite

The spatial variations of S isotopes and relative abundances of trace elements such as Au, As and Cu across Py-2 and Py-3, determined by *in-situ* NanoSIMS, are illustrated in Figs. 6–8. Similar to results for Au-bearing arsenian pyrite from the Nevada Carlin-type Au deposits (Barker et al., 2009), Au-bearing arsenian pyrite from Lannigou are also characterized by nanoscale chemical and isotopic zonation. Another new and interesting observation is that the $\delta^{34}S$ values and Au

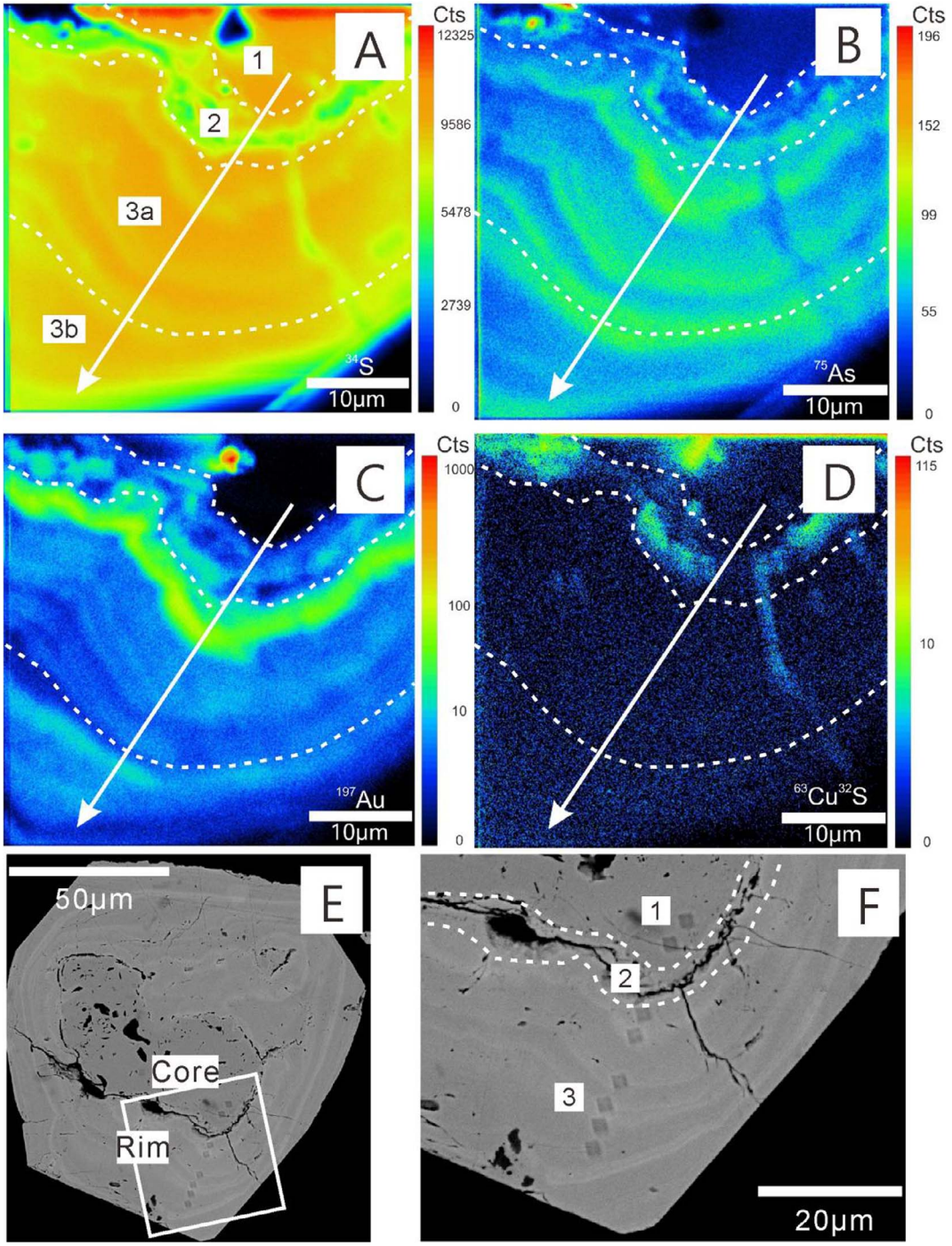

Fig. 7. NanoSIMS elements mapping of representative pyrite from sample LNG3-11, Lannigou gold deposit. LNG3-11 is collected at ore heap from underground with 250 ~ 370m level. (A-D) elements mapping, (E-F) BSE of analyzed pyrite. Similar with pyrite in Fig. 5, three main stage also can be found in this pyrite. Color scale of (A-B) are linear and (C-D) are log due to lower Au and Cu concentration. Frame in (E) is element mapping area. The white arrow denotes the path of line scan shown in Fig. 8B.

concentrations in the Au-bearing arsenian pyrite from Lannigou are negatively correlated (Fig. 8A). $\delta^{34}S$ variation line in Fig. 8A was determined by spots $\delta^{34}S$ analyses as shown in Fig. 9C.

Based on the outward oscillatory distribution patterns of Au and As across individual pyrite grains in the samples collected from both the upper part (open-pit at 500–520 m elevation) and the lower part (underground mining tunnel at 250–370 m elevation) of the orebody associated with the F3 and F6 fault in Lannigou, a total of three major crystal growth stages were observed (Figs. 6 and 7). Stage 1 is represented by Py-1 and Au-free and As-poor (< 0.65 wt%) core of Py-2. The rim of Py-2 is divided into stage 2 and stage 3 (outwards). Stage 2 is characterized by being As-rich (< 8.2 wt%) and Au-free (Fig. 6C), or low-Au (Fig. 7C). Stage 3 is the main Au precipitation stage, characterized by high concentrations of As (1.38–7.88 wt%) and Au (< 0.28 wt%). The Au/As atomic ratio of the pyrite rim varies from below 1:1000 to near 1:10 (Fig. 5C). However, spots of stage 2 are mostly filled into lower Au/As ratio zone and spots of Stage 3 are with higher Au/As atom ratio. The major and minor elements features of each stage are shown in Table 2 and Fig. 5.

Stage 3 can be further divided into two sub-stages: stage 3a with higher Au/As atom ratio and a positive Au-As correlation, and stage 3b with lower Au/As atom ratio and a negative Au-As correlation

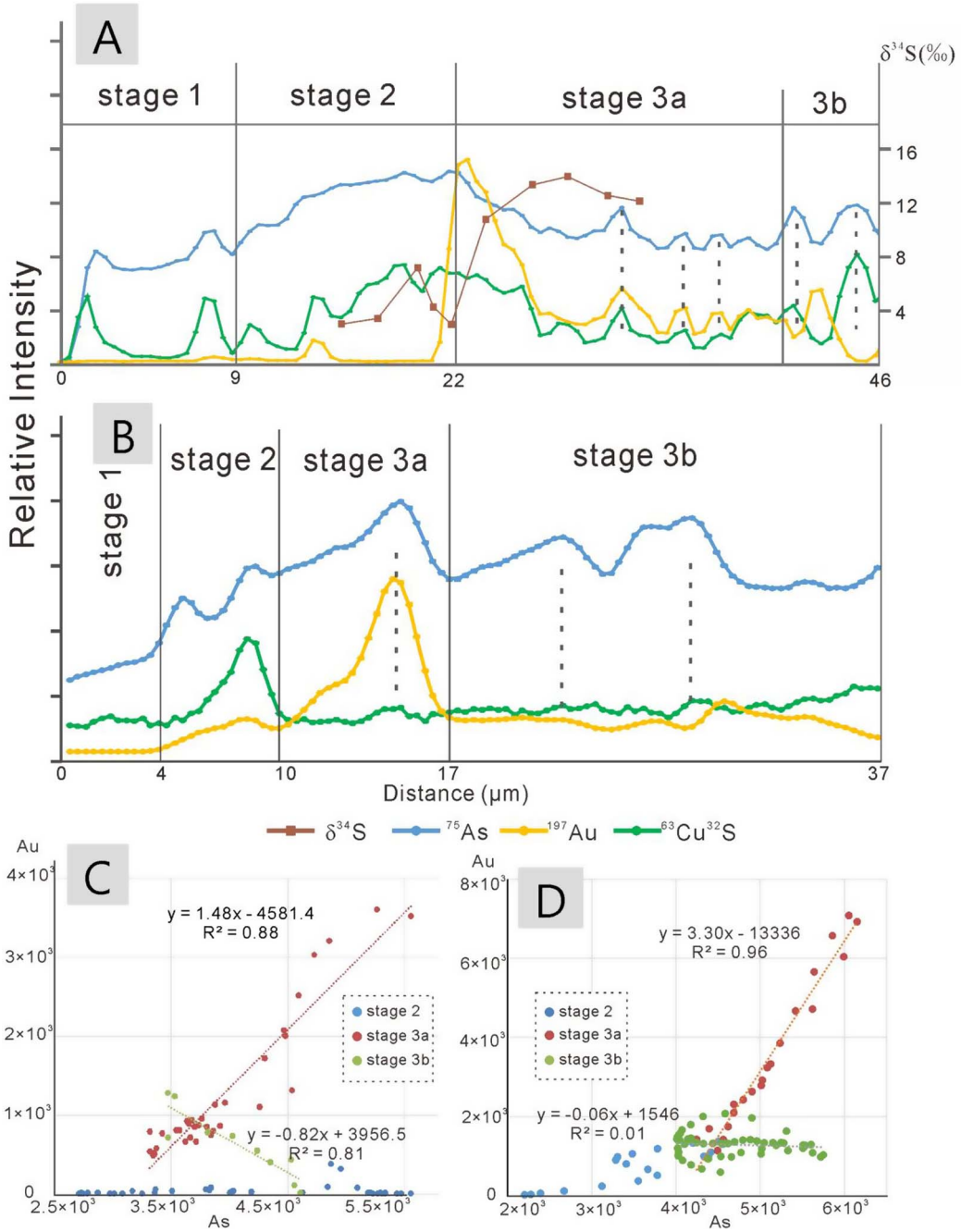

Fig. 8. (A) Elements line scan and $\delta^{34}S$ variation of representative pyrite from LNG3-1 (scan path in Fig. 6). The $\delta^{34}S$ values are analyzed after elements mapping in same pyrite rim, and plotted according to their locations (Fig. 9C). The $\delta^{34}S$ is negatively correlated with Au and As. (B) Line scan of representative pyrite from LNG3-11 (scan path in Fig. 7). (C) (D) Linear fitting of Au-As relationship in each stage of scanned pyrites in (A) (B), respectively. The dashed line in (A) (B) shows positive correlation of As and Cu during mineralization, positive relationship of Cu and Au in stage 3a and negative correlation in stage 3b. Linear fittings in (C) (D) reveal that the positive and negative relationship between Au and As in stage 3a and stage 3b both occur at samples from open pit and underground.

(Figs. 5C and 8). A positive correlation between Cu and As concentrations is present during the entire mineralization process (Figs. 5B and 8A and B).

4.3. $\delta^{34}S$ variation within a single pyrite grain and between coexisting sulfides

The variation of $\delta^{34}S$ values within 14 individual pyrite crystals from 6 hand specimens, determined by *in-situ* NanoSIMS is illustrated in Fig. 9E. The analytical results, together with those for 11 sulfide separates (stibnite, realgar, cinnabar) from 10 hand specimens, determined by MAT-253 mass spectrometer, are listed in Table 3 and Appendix III.

There is significant variation of $\delta^{34}S_{CDT}$ values from the core to rim in Au-bearing pyrite (Py-2) (Fig. 9). Zones representing stages 1, 2 and 3 of the Au-bearing pyrite have $\delta^{34}S_{CDT}$ range from 6.0 to 11.5‰, 1.1 to 7.9‰, and 4.9 to 18.1‰, respectively (Table 3, Fig. 9E). Across a single grain, the $\delta^{34}S_{CDT}$ values generally increase outward from stage 2 to stage 3 zones. Some rims of Au-bearing pyrite grains have smaller range of $\delta^{34}S_{CDT,}$ such as those from sample LNG3-8 (4.9–7.9‰) (Fig. 9A) and LNG3-11 (10.3–15.4‰) (Fig. 9D). In contrast, some rims of other pyrite grains have larger ranges of $\delta^{34}S_{CDT,}$ such as those from samples LNG3-9 (2.0–10.2‰) (Fig. 9B) and LNG3-1 (2.7–13.9‰) (Fig. 9C). In disparity, those formed prior to Au deposition (i.e., Py-1 and core of Py-2) such as those from sample LNG6-1 have high and restricted $\delta^{34}S_{CDT}$

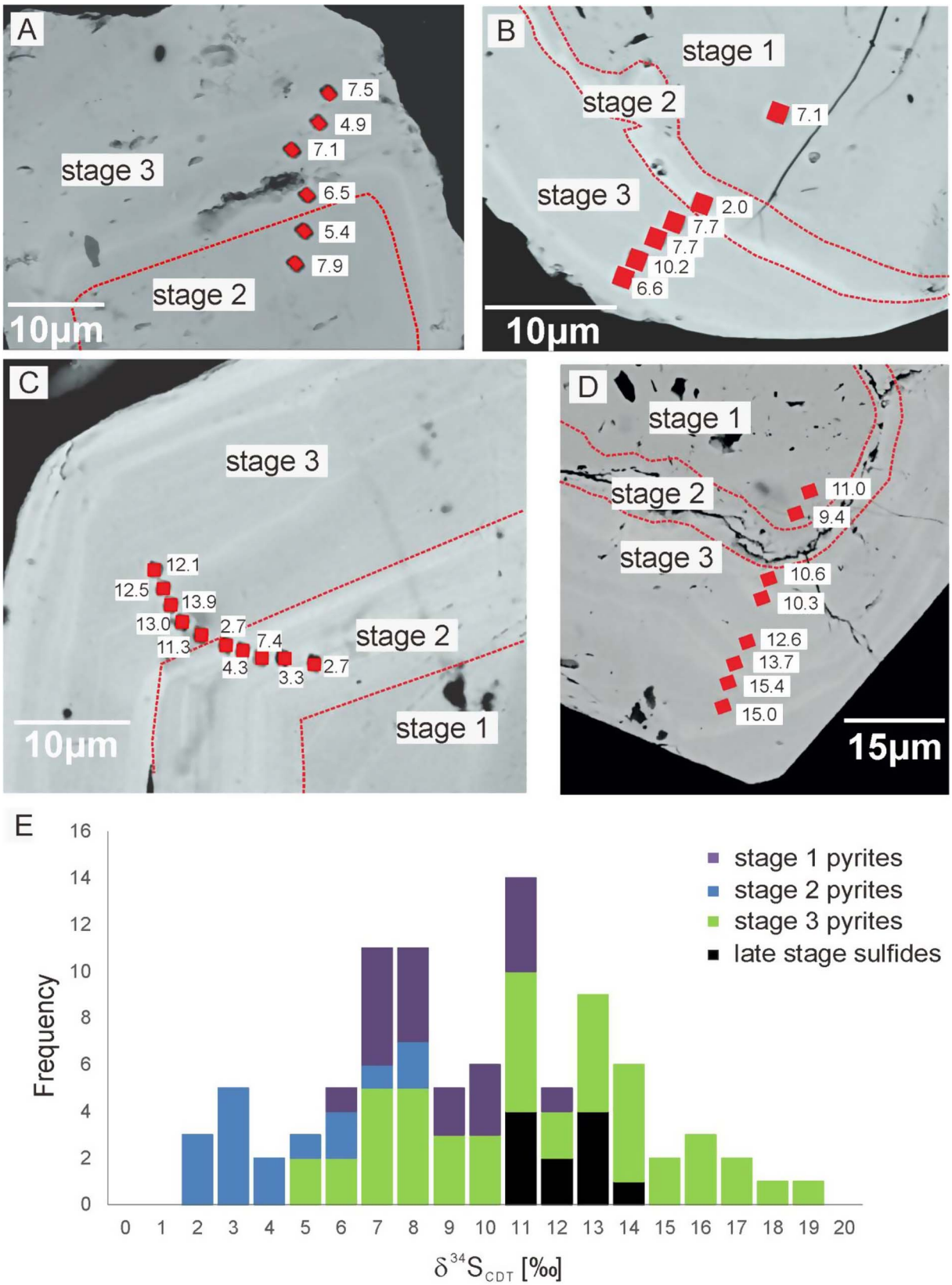

Fig. 9. The $\delta^{34}S$ of representative pyrites from LNG3-8(A), LNG3-9(B), LNG3-1(C), LNG3-11(D). (E) The $\delta^{34}S$ histogram of different stages pyrites and late sulfides. Stage 1 to stage 3 represented pre-ore stage, early mineralization stage, and gold precipitation stage, respectively.

values close to 11‰.

Other sulfide minerals such as realgar, cinnabar and stibnite that formed after the stages of Au deposition all have high $\delta^{34}S_{CDT}$ values varying between 10.6 and 13.2‰. The range of $\delta^{34}S_{CDT}$ for each mineral is more restricted and are as follows: 12.2–13.2‰ for realgar, 10.7–12.0‰ for cinnabar, and 10.7–10.8‰ for stibnite. Using the isotope fractionation

Table 3
$\delta^{34}S$ range of different stages pyrites by in-situ NanoSIMS and late stage single sulfide minerals by IRMS. n = number of analyzed spots.

	n	Minerals	$\delta^{34}S_{CDT}$[‰] range	Mean $\delta^{34}S_{CDT}$[‰]	1SD
Stage 1	20	Pyrite	6.1–11.5	8.3	1.8
Stage 2	14	Arsenic pyrite	1.1–7.9	3.8	2.0
Stage 3	45	Arsenic pyrite	4.9–18.1	10.7	3.6
Late stage	11	Late sulfides	10.6–13.2	11.7	0.9

equation of $\delta^{34}S_{cinnabar} - \delta^{34}S_{stibnite} = 0.05 \times (10^6/T^2)$ from Ohmoto and Rye (1979), our results for these two minerals from the deposit yield an apparent temperature of 6 °C. This temperature is too low and unrealistic, indicating that these minerals were not formed at the same time.

5. Discussion

S-isotope signatures of the sulfides and the Au/As ratio of arsenian pyrite might be used to track hydrothermal fluid evolution under different physicochemical conditions (Ohmoto, 1972; Deditius et al., 2014). Based on mineral textures and assemblages, trace element distribution in pyrite, S isotopes of pyrite crystals determined by *in-situ* method and S isotopes of other sulfides determined by conventional method, the fluid evolution during mineralization can be divided into 4 stages with different fluid compositions. The fluid involved in the early stages (the entire grain of Py-1 and the Au-free core of Py-2) did not contain significant amount of Au. The latter fluids that were involved in the formation of Py-2 rim and Py-3 were all Au-bearing, with increasing Au and As concentrations with time. The last fluid (late stage) that was involved in the formation of other sulfide minerals such as realgar, cinnabar and stibnite also did not carry significant amount of Au.

5.1. Modes of occurrence of Au in pyrite

Iron in Au-bearing pyrite from Carlin-type Au deposits is widely considered to be derived from siliceous carbonate wall-rocks by decarbonization and sulfidization during rock-fluid interaction, whereas S in the pyrite and other associated trace elements such as Au, As and Cu are mainly derived from the hydrothermal fluids (Hofstra et al., 1991; Hu et al., 2002; Kesler et al., 2003; Su et al., 2009a; Deditius et al., 2014). The modes of occurrence of the trace elements, especially Au in the pyrite, however, still remain elusive, mainly due to the limitation of analytical sensitivity or spatial resolution of the methods used in the past such as EMPA, LA-ICP-MS and SIMS (Cline, 2001; Emsbo et al., 2003; Zhang et al., 2003; Reich et al., 2005; Muntean et al., 2011; Su et al., 2012; Deditius et al., 2014).

Our data for the Au-bearing pyrite in the Lannigou Carlin-type Au deposit in SW China show a lack of linear correlation between Au and As (Figs. 4A and 5A). As shown in Fig. 5C, the Au/As ratio in the rim of the pyrite varies from 1:1000 to 1:10, corresponding to a change of this ratio up to two orders of magnitude. Many spots are over the limit line of Au solubility (Reich et al., 2005), or fall into the field of Au nanoparticles/Au^+ (Deditius et al., 2014). Because As occurs in the crystal structure substituting for S (Fig. 4D), such magnitude of change at both the submicron and nanoscales indicates that unlike As, most of the Au must occur as nanoparticles rather than in the crystal lattice. This interpretation is similar to that of Deditius et al. (2014) who studied other gold deposits in the world.

5.2. Implications for the precipitation mechanism of Au

The Au/As ratios in the stage 2 zone of the Au-bearing pyrite from Lannigou are extremely low due to high As and low Au concentrations, and might take major responsibility for nonsystematic Au-As relationship. The contents of Au in this zone are mostly below the detection limit of EPMA and NanoSIMS (Figs. 5–8). As pointed out previously by some researchers (Bowers, 1991; Simon et al., 1999; Loucks and Mavrogenes, 1999), these characteristics may have been caused by the pH fluctuation associated with the following reactions that control formation of arsenian pyrite and precipitation of Au at the same time:

$$1/3H_3As_3S_6 + Au(HS)_2^- + Fe^{2+} + 3/2H_2 = Fe(SAs){-}Au(HS)^0 + 2H_2S + H^+, \quad (1)$$

$$Fe(S,As)_2 + Au(HS)_2^- = Fe(S,As)_2{-}Au(HS)^0 + HS^- \quad (2)$$

The above reactions are coupled with the following reactions that control Au precipitation from the ore-forming hydrothermal fluid:

$$Au(HS)_2^- + 2H^+ = Au^+_{(PY)} + 2H_2S, \quad (3)$$

or

$$Au(HS)_2^- + 1/2H_2 + H^+ = Au^0 + 2H_2S. \quad (4)$$

The increase in pH in the fluid is thought to be associated with decarbonization and loss of CO_2 and H_2S *via* the following reactions:

$$CaCO_3 + 2H^+ = Ca^{2+} + H_2O + CO_2, \quad (5)$$

$$H^+ + HCO_3^- = H_2O + CO_2, \quad (6)$$

$$H^+ + HS^- = H_2S. \quad (7)$$

At the early stages of rock-fluid interaction involving reactions (1) (5), substantial amounts of H^+ ions are consumed by the decarbonization process (5). The release of H_2S and CO_2 by reactions (6) and (7) accelerates reactions (1) and (2), and thus promotes co-precipitation of arsenian pyrite and Au from the fluid. However, the increase of pH (H^+ loss) for the fluid causes a reversal for reactions (3) and (4), hereby increasing the solubility of Au in the fluid and consequently limiting Au precipitation with arsenian pyrite (Stage 2 in Figs. 6C, 7C and 8).

Palenik et al. (2004) suggested that efficient scavenging of Au from ore fluid is dominated by the kinetics of pyrite precipitation rather than equilibrium partitioning. Based on previously reported mineralogical features of Carlin pyrite (e.g., nano-particulate As-rich rims, nonsystematic distribution of Au), Deditius et al. (2014) suggested that surface kinetics especially Fe-vacancies might be a major cause of Au and other trace element precipitation. However, the results of NanoSIMS mapping reveal the highest Au concentration rim in stage 3a subzone and rhythmic Au zoning of the Au-bearing pyrites (Fig. 6C, 7C and 8A and B). These features of Au distribution indicate that multiple influx of Au-bearing fluid generated episodic Au precipitation. The stage 3a Au-rich subzone of pyrite both in shallow and deep samples all show good positive Au-As correlation (Fig. 8C and D), indicating that arsenian pyrite crystallization and Au precipitation took place at the same time during this stage, perhaps controlled by reaction (1) above. The decoupling between Au and As in the stage 3b subzone of pyrites implies decreasing Au concentration in the fluid at this stage. We do not have the clear answer to this observation yet. However, what is quite clear is that the ore-forming hydrothermal systems remained open for a long time or secondary thermal perturbation took place repeatedly.

With the progress of decarbonization and the formation of clay minerals such as illite, pH and fO_2 could increase significantly in the ore-forming fluids of the Lannigou Carlin-type Au deposit (Zhang et al., 2003; Hu et al., 2002; Su et al., 200a). As a result, Au could occur mainly as Au^{3+} ions, similar to high-sulfidation epithermal Au systems (Simon et al., 1999; Deditius et al., 2008; Qian et al., 2013). In this case, Au could enter the pyrite crystal lattice as Au^{3+}, competing with Cu^{2+}. The involvement of this process might explain negative Au-Cu correlations at stage 3b (Figs. 6D and 8A).

5.3. Controls on S isotope variation

Sulfur isotope of minerals might be influenced by significant pressure dropping, especially decompression boiling. This decompression also called flash vaporization will lead to abundant metal precipitation (Weatherley and Richard, 2013; Peterson and Mavrogenes, 2014). During boiling, the lighter ^{32}S will go to the vapor phase and the heavier ^{34}S will remain in the residual fluid, resulting in an increase in $\delta^{34}S$. However, this process is unlikely to be the main reason for the increasing of $\delta^{34}S$ across the Au-bearing pyrite crystals of the deposit, because no evidence for fluid boiling has been found for this deposit (Hu et al., 2002; Zhang et al., 2003; Su et al., 2009a). Based on fluid inclusion studies (Zhang et al., 2003), the forming temperature of the deposit was estimated to be between 150 and 300 °C. At depths of 5.5–8.9 km (corresponding to a total pressure of < 2.3 kbar), no fluid boiling is expected. Evidence from the NanoSIMS line scans of Au-bearing pyrite also argue against decompression boiling: Au, As and Cu peaks in Fig. 8A are coincide with $\delta^{34}S$ troughs rather than $\delta^{34}S$ peaks.

If barite is also present, the changes of fO_2 and pH in the fluid could also affect the S isotope composition of pyrite due to S isotope fractionation between these two phases, as well as the effect of these variables on the sulfide-sulfate phase transition (Ohmoto, 1972). However, no barite and other sulfates have been found in the Lannigou Carlin-type Au deposit. The effect of changing fO_2 and pH on the variation of $\delta^{34}S$ in the Au-bearing pyrite of the Lannigou Carlin-type Au deposit could not be significant.

Sulfur isotopes in hydrothermal pyrite crystals are a function of fluid temperature. The S isotope fractionation factor between pyrite and a hydrothermal fluid [$\Delta(\delta^{34}S_{FeS2}–\delta^{34}S_{H2S})$] is negatively correlated with temperature and can reach 2‰ at temperature varying in ~100 °C (Ohmoto, 1972). Heat loss to the ambient country rocks coupled with periodic replenishment of hotter hydrothermal fluid could cause the temperature of the ore-forming fluid to fluctuate. This, together with different S isotope compositions between the resident fluid and the new input, could cause significant fluctuation of S isotope compositions for a hybrid fluid and the pyrite crystallizing from it.

5.4. Fluid and sulfur sources

Our new S isotope compositions for the Au-bearing arsenian pyrite of the Lannigou Carlin-type Au deposit determined by *in-situ* NanoSIMS (1.1–18.1‰, Table 3, Fig. 9E) encompass those for sedimentary pyrite in the country rocks (~11.8‰; Hu et al., 2002; Zhang et al., 2003; Chen et al., 2015b). Based on the ore fluid stages defined above, the data also shows that $\delta^{34}S$ values of ore fluid generally increase during gold mineralization (1.1–7.9‰ in Stage 2 to 4.9–18.1‰ in Stage 3) and back to 10.6–13.2‰ at the late stage closed to the sedimentary country rocks (Fig. 9E). These characteristics are interpreted to show fluid-mixing of multiple end-members as discussed above. The similarity and difference of $\delta^{34}S$ values between mineralization fluid and sedimentary country rocks are consistent with the interpretation that pyrite in the country rocks are a major sulfur source for the deposit. However, another distinct source with much lower $\delta^{34}S$ values is required to explain lower $\delta^{34}S$ values for some of the Au-bearing arsenian pyrites in the deposit. Since contemporaneous granitic plutons are present in the greater Golden Triangle region, we propose that a granite-derived magmatic-related hydrothermal fluid with $\delta^{34}S$ value close to the mantle value (i.e., close to zero) was the second source of sulfur involved in deposit formation. Mixing between these two different sources at different proportions, as well as the different temperatures of the mixed fluid can well explain the observed large variation of $\delta^{34}S$ for the Au-bearing pyrite in the deposit. Samples with larger ranges of $\delta^{34}S$ values such as LNG3-9-2-02 (2.0–10.2‰, Fig. 9B) and LNG3-1-1-1 (2.7–13.9‰, Fig. 9C) are consistent with larger change in the proportions of these two end-members during formation. Samples with smaller ranges of $\delta^{34}S$ values such as LNG3-8-2-1 (4.9–7.9‰, Fig. 9A) and LNG3-11-2-1 (10.3–15.4‰, Fig. 9D) are consistent with smaller variation in the proportions of these two end-members during the formation of the Au-bearing pyrite crystals in the deposit. The nanoscale peaks of Au and As line scan are coupled with valleys of $\delta^{34}S$ values (Fig. 8A), indicating that the end-member with low $\delta^{34}S$ is likely also characterized by high Au, As content.

It is possible that basin brines, which were recently found in the vicinity of the Lannigou Carlin-type Au deposit, was an alternative source of the crustal fluid involved in the formation of the deposit due to basin geological background in this region (Gu et al., 2012). The brine is known to contain high abundances of bitumen and organic components that are also present in the fluid inclusions of the deposits accompanied with high $\delta^{34}S$ value that can explain the elevated $\delta^{34}S$ value (18.1‰) in some gold-bearing pyrite crystals. However, no direct S isotope data are available for such brines.

6. Conclusions

NanoSIMS line scans reveal complex Au-As relationships during the growth of Au-bearing pyrite in the Lannigou Carlin-type Au deposit, indicating an open hydrothermal ore-forming system for the deposit. NanoSIMS line scans reveal that the peaks of As concentration at the nanoscale is coupled with valleys in $\delta^{34}S$, indicating that the change in chemical composition of the fluid played a bigger role than the change in the temperature of the fluid in the observed elemental and isotope fractionation. Comparison of the $\delta^{34}S$ values between the deposit and the sedimentary rocks reveals that the Au-bearing fluid was likely formed by the mixing between an As-rich magmatic fluid with mantle-like $\delta^{34}S$ and a crustal fluid with elevated $\delta^{34}S$. Sulfur in the crustal fluid is likely to have derived from the sedimentary pyrite in the country rocks via fluid-rock interaction. The change in the proportions of these two end-members are likely the main reason for the changes of Au-As-Cu concentrations and S isotope compositions at different scales from different depths to different zones of individual Au-bearing pyrite crystals.

Acknowledgements

This research was jointly funded by the key project of National Natural Science Foundation of China (41230316) and the National 973 Program of China (2014CB440906). We thank Jinfeng Mine Ltd for field work support, Dr. Shaohua Dong for assistance in SEM analysis, Prof. Minwu Liu for assistance in EPMA analysis, and Dr. Lin An for assistance in S isotope analyses of sulfide separates. We are indebted to Dr. Wenchao Su for his insightful comments and useful suggestions, and to Dr. Chusi Li of Indiana University for his carefully editing for both science and language. The manuscript benefitted from thoughtful reviews and language advancement by Prof. Nigel Cook and another anonymous reviewer, to whom we are grateful.

Appendix A. Supplementary data

Supplementary data associated with this article can be found, in the online version, at http://dx.doi.org/10.1016/j.oregeorev.2017.10.015.

References

Arehart, G.B., Chryssoulis, S.L., Kesler, S.E., 1993. Gold and arsenic in iron sulfides from sediment-hosted disseminated gold deposits: implications for depositional processes. Econ. Geol. 88, 171–185.

Arehart, G.B., 1996. Characteristics and origin of sediment-hosted disseminated gold deposits: a review. Ore Geol. Rev. 11, 383–403.

Barker, S., Hickey, K.A., Cline, J.S., Dipple, G.M., Kilburn, M.R., Vaughan, J.R., Longo, A.A., 2009. Uncloaking invisible gold: use of nanosims to evaluate gold, trace elements, and sulfur isotopes in pyrite from carlin-type gold deposits. Econ. Geol. 104, 897–904.

Bowers, T.S., 1991. The deposition of gold and other metals: pressure-induced fluid immiscibility and associated stable isotope signatures. Geochim. Cosmochim. Acta 55,

2417–2434.
Chen, M.H., Mao, J.W., Frank, P.B., Tony, N., Uttley, P.J., 2011. Structural features and metallogenesis of the Carlin-type Jinfeng (Lannigou) gold deposit, Guizhou Province, China. Ore Geol. Rev. 43, 217–234.
Chen, M.H., Mao, J.W., Li, C., Zhang, Z.Q., Dang, Y., 2015a. Re–Os isochron ages for arsenopyrite from Carlin-like gold deposits in the Yunnan–Guizhou–Guangxi "golden triangle", southwestern China. Ore Geol. Rev. 64, 316–327.
Chen, M.H., Zhang, Z.Q., Santosh, M., Dang, Y., Zhang, W., 2015b. The Carlin-type gold deposits of the "golden triangle" of SW China: Pb and S isotopic constraints for the ore genesis. J. Asian Earth Sci. 103, 115–128.
Cline, J.S., 2001. Timing of gold and arsenic sulfide mineral deposition at the Getchell Carlin-type gold deposit, North-Central Nevada. Econ. Geol. 96, 75–89.
Cline, J.S., Hofstra, A.H., Muntean, J.L., Tosdal, R.M., Hickey, K.A., 2005. Carlin-type gold deposits in Nevada: Critical geological characteristics and viable models. Econ. Geol. 100TH Anniversary Volume 451–484.
Deditius, A.P., Utsunomiya, S., Renock, D., Ewing, R.C., Ramana, C.V., Becker, U., Kesler, S.E., 2008. A proposed new type of arsenian pyrite: composition, nanostructure and geological significance. Geochim. Cosmochim. Acta 72, 2919–2933.
Deditius, A.P., Reich, M., Kesler, S.E., Utsunomiya, S., Chryssoulis, S.L., Walshe, J., Ewing, R.C., 2014. The coupled geochemistry of Au and As in pyrite from hydrothermal ore deposits. Geochim. Cosmochim. Acta 140, 644–670.
Emsbo, P., Hofstra, A.H., Lauha, E.A., Griffin, G.L., Hutchinson, R.W., 2003. Origin of high-grade gold ore, source of ore fluid components, and genesis of the Miekle and neighboring Carlin-type deposits, Northern Carlin Trend, Nevada. Econ. Geol. 98, 1069–1105.
Gu, X.X., Zhang, Y.M., Li, B.H., Dong, S.Y., Xue, C.J., Fu, S.H., 2012. Hydrocarbon- and ore-bearing basinal fluids: a possible link between gold mineralization and hydrocarbon accumulation in the Youjiang basin, South China. Miner. Deposita 47, 663–682.
Hofstra, A.H., Leventhal, J.S., Northrop, H.R., Landis, G.P., Rye, R.O., Birak, D.J., Dahl, A.R., 1991. Genesis of sediment-hosted disseminated-gold deposits by fluid mixing and sulfidization: chemical-reaction-path modeling of ore-depositional processes documented in the Jerritt Canyon district, Nevada. Geology 19, 36–40.
Hofstra, A.H., Cline, J.S., 2000. Characteristics and models for Carlin-type gold deposits. In: Hagemann, S.G., Brown, P.E. (Eds.), Gold in 2000: Reviews in Economic Geology 13, pp. 163–220.
Hu, R.Z., Su, W.C., Bi, X.W., Tu, G.Z., Hofstra, A.H., 2002. Geology and geochemistry of Carlin-type gold deposits in China. Miner. Deposita 37, 378–392.
Hu, R.Z., Zhou, M.F., 2012. Multiple Mesozoic mineralization events in South China—an introduction to the thematic issue. Miner. Deposita 47, 579–588.
Hu, R.Z., Fu, S.L., Huang, Y., Zhou, M.F., Fu, S.H., Zhao, C.H., Wang, Y.J., Bi, X.W., Xiao, J.F., 2017. The giant South China Mesozoic low-temperature metallogenic domain – reviews and a new geodynamic model. J. Asian Earth Sci. 137, 9–34.
Kesler, S.E., Fortuna, J., Ye, Z., Alt, J.C., Core, D.P., Zohar, P., Borhauer, J., Chryssoulis, S.L., 2003. Evaluation of the role of sulfidation in deposition of gold, Screamer section of the Betze-Post Carlin-type deposit, Nevada. Econ. Geol. 98, 1137–1157.
Kesler, S.E., Riciputi, L.C., Ye, Z.J., 2005. Evidence for a magmatic origin for Carlin-type gold deposits: isotopic composition of sulfur in the Betze-Post-Screamer Deposit, Nevada, USA. Miner. Deposita 40, 127–136.
Large, R.R., Danyushevsky, L., Hollit, C., Maslennikov, V., Meffre, S., Gilbert, S., Bull, S., Scott, R., Emsbo, P., Thomas, H., Singh, B., Foster, J., 2009. Gold and trace element zonation in pyrite using a laser imaging technique: implications for the timing of gold in orogenic and carlin-style sediment-hosted deposits. Econ. Geol. 104, 635–668.
Large, R.R., Bull, S., Maslennikov, V., 2011. A carbonaceous sedimentary source-rock model for carlin-type and orogenic gold deposits. Econ. Geol. 106, 331–358.
Loucks, R.R., Mavrogenes, J.A., 1999. Gold solubility in supercritical hydrothermal brines measured in synthetic fluid inclusions. Science 284, 2159–2163.
Lubben, J.D., Cline, J.S., Barker, S., 2012. Ore fluid properties and sources from quartz-associated gold at the Betze-post carlin-type gold deposit, Nevada, United States. Econ. Geol. 107, 1351–1385.
Mao, J.W., Cheng, Y.B., Chen, M.H., Pirajno, F., 2013. Major types and time- space distribution of Mesozoic ore deposits in South China and their geodynamic settings. Miner. Deposita 48, 267–294.
Muntean, J.L., Cline, J.S., Simon, A.C., Longo, A.A., 2011. Magmatic–hydrothermal origin of Nevada's Carlin-type gold deposits. Nat. Geosci. 4 (2), 12–127.
Ohmoto, H., 1972. Systematics of sulfur and carbon isotopes in hydrothermal ore deposits. Econ. Geol. 67, 551–578.
Ohmoto, H., Rye, R.O., 1979. Isotopes of sulfur and carbon. In: Barnes, H.L. (Ed.), Geochemistry of Hydrothermal Ore Deposits, second ed. Wiley-Interscience, New York, NY, pp. 509–567.
Palenik, C.S., Ustunomiya, S., Reich, M., Kesler, S.E., Wang, L., Ewing, R.C., 2004. "Invisible" gold revealed: direct imagining of gold nanoparticles in a Carlin-type deposit. Am. Miner. 89, 1359–1366.
Peters, S.G., Huang, J.Z., Li, Z.P., Jing, C.G., 2007. Sedimentary rock-hosted Au deposits of the Dian–Qian–Gui area. Ore Geol. Rev. 31, 170–204.
Peterson, E.C., Mavrogenes, J.A., 2014. Linking high-grade gold mineralization to earthquake-induced fault-valve processes in the Porgera gold deposit, Papua New Guinea. Geology 42, 383–386.
Pi, Q.H., Hu, R.Z., Xiong, B., Li, Q.L., Zhong, R.C., 2017. In situ SIMS U-Pb dating of hydrothermal rutile: reliable age for the Zhesang Carlin-type gold deposit in the golden triangle region, SW China. Miner. Deposita. http://dx.doi.org/10.1007/s00126-017-0715-y.
Price, J.G., et al., 2008. The Nevada Minerals Industry 2007. Nevada Bureau of Mines and Geology Special Publication MI-2007.
Qian, G., Brugger, J., Testamale, D., Skiner, W., Pring, A., 2013. Formation of As(II)-pyrite during experimental replacement of magnetite under hydrothermal conditions. Geochim. Cosmochim. Acta 100, 1–10.
Reich, M., Kesler, S.E., Utsunomiya, S., Palenik, C.S., Chryssoulis, S.L., Ewing, R.C., 2005. Solubility of gold in arsenian pyrite. Geochim. Cosmochim. Acta 69, 2781–2796.
Simon, G., Kesler, S.E., Chryssoulis, S., 1999. Geochemistry and texture of gold-bearing Arsenian pyrite, twin creeks, nevada: implication for deposition of Gold in carlin-type deposits. Econ. Geol. 94, 405–422.
Su, W.C., Xia, B., Zhang, H.T., Zhang, X.C., Hu, R.Z., 2008. Visible gold in arsenian pyrite at the Shuiyindong Carlin-type gold deposit, Guizhou, China: implications for the environment and processes of ore formation. Ore Geol. Rev. 33, 667–679.
Su, W.C., Heinrich, C.A., Pettke, T., Zhang, X.C., Hu, H.R., Xia, B., 2009a. Sediment-hosted gold deposits in Guizhou, China: products of wallrock sulfidation by deep crustal fluids. Econ. Geol. 104, 73–93.
Su, W.C., Hu, R.Z., Xia, B., Xia, Y., Liu, Y.P., 2009b. Calcite Sm-Nd isochron age of the Shuiyindong Carlin-type gold deposit, Guizhou, China. Chem. Geol. 258, 269–274.
Su, W.C., Zhang, H.T., Hu, R.Z., Ge, X., Xia, B., Chen, Y.Y., Zhu, C., 2012. Mineralogy and geochemistry of gold-bearing arsenian pyrite from the Shuiyindong Carlin-type gold deposit, Guizhou, China: implications for gold depositional processes. Miner. Deposita 47, 653–662.
Tu, G., 1990. The SW Qinling and the SW Guizhou uranium and gold metallogenic belts, and their similarities to the Carlin-type gold deposits in the western states, USA. Uranium Geol. 6, 321–325 (in Chinese with English abstract).
Tu, G., 1992. Some problems on prospecting of super large gold deposits. Acta Geol. Sichuan Spec. Issue 12, 1–9 (in Chinese with English abstract).
Wang, G.Z., Hu, R.Z., Su, W.c., Zhu, L.M., 2003. Fluid flow and mineralization of Youjiang Basin in the Yunnan-Guizhou-Guangxi area, China. Sci. China (Series D) 46, 99–109.
Wang, Y.J., Fan, W.M., Sun, M., Liang, X.Q., Zhang, Y.H., Peng, T.P., 2007. Geochronological, geochemical and geothermal constraints on petrogenesis of the Indosinian peraluminous granites in the South China Block: a case study in the Hunan Province. Lithos 96, 475–502.
Weatherley, D.K., Richard, W.H., 2013. Flash vaporization during earthquakes evidenced by gold deposits. Nat. Geosci. 6 (4), 294–298.
Xie, Z.J., Xia, Y., Cline, J.S., Yan, B.W., Wang, Z.P., Tan, Q.P., Wei, D.T., 2017. Comparison of the native antimony-bearing Paiting gold deposit, Guizhou Province, China, with Carlin-type gold deposits, Nevada, USA. Miner. Deposita 52 (1), 69–84.
Zhang, J.C., Lin, Y.T., Yang, W., Shen, W.J., Hao, J.L., Hua, S., Cao, M.J., 2014. Improved precision and spatial resolution of sulfur isotope analysis using NanoSIMS. J. Anal. At. Spectrom. 29, 1934–1943.
Zhang, X.C., Spiro, B., Halls, C., Stanley, C.J., Yang, K.Y., 2003. Sediment-hosted disseminated gold deposits in Southwest Guizhou, PRC: their geological setting and origin in relation to mineralogical, fluid inclusion, and stable-isotope characteristics. Int. Geol. Rev. 45, 407–470.
Zhou, X.M., Sun, T., Shen, W.Z., Shu, L.S., Niu, Y.L., 2006. Petrogenesis of mesozoic granitoids and volcanic rocks in South China: a response to tectonic evolution. Episodes 29, 26–33.
Zhu, J.J., Hu, R.Z., Richards, J.P., Bi, X.W., Stern, R., Lu, G., 2017. No genetic link between Late Cretaceous felsic dikes and Carlin-type Au deposits in the Youjiang basin, Southwest China. Ore Geol. Rev. 84, 328–337.